

Bottom-Up Human Pose Estimation by Ranking Heatmap-Guided Adaptive Keypoint Estimates

Ke Sun, Zigang Geng, Depu Meng, Bin Xiao, Dong Liu, Zhaoxiang Zhang, Jingdong Wang

Abstract—The typical bottom-up human pose estimation framework includes two stages, keypoint detection and grouping. Most existing works focus on developing grouping algorithms, e.g., associative embedding, and pixel-wise keypoint regression that we adopt in our approach. We present several schemes that are rarely or unthoroughly studied before for improving keypoint detection and grouping (keypoint regression) performance. First, we exploit the keypoint heatmaps for pixel-wise keypoint regression instead of separating them for improving keypoint regression. Second, we adopt a pixel-wise spatial transformer network to learn adaptive representations for handling the scale and orientation variance to further improve keypoint regression quality. Last, we present a joint shape and heatvalue scoring scheme to promote the estimated poses that are more likely to be true poses. Together with the tradeoff heatmap estimation loss for balancing the background and keypoint pixels and thus improving heatmap estimation quality, we get the state-of-the-art bottom-up human pose estimation result. Code is available at <https://github.com/HRNet/HRNet-Bottom-up-Pose-Estimation>.

Index Terms—Bottom-Up Pose Estimation, Adaptive Representation Transformation, Pose Scoring, Tradeoff Heatmap Estimation Loss.



1 INTRODUCTION

HUMAN pose estimation aims to predict the keypoint positions of each person from an image, i.e., localize the keypoints as well as identify the person the keypoints belong to. It has broad applications, including action recognition, person re-identification, pedestrian tracking, human-computer interaction, smart photo editing, etc. A lot of techniques have been developed to deal with various challenges as depicted in Figure 1, such as unknown number of persons, diverse person scales and orientations, various poses, and so on.

There are two main frameworks top-down and bottom-up. The top-down framework first detects the person and then performs single-person pose estimation for each detected person. The bottom-up framework first predicts the keypoint positions and then groups the keypoints into individuals. The former is more accurate but more costly, and the latter is more efficient and less accurate. This paper focuses on the latter one and improving the pose estimation accuracy.

The typical bottom-up framework consists of two steps. The first step is to estimate keypoint heatmaps, where each position in each keypoint heatmap has a value indicating the degree that the keypoint lies in the position. The second step is to group the detected keypoints, identified in the first step, into persons. Most existing works mainly focus on the second step. The representative works include affinity linking [2], [13], associative embedding [23], pixel-wise keypoint regression [45], and so on. We adopt the pixel-wise keypoint regression scheme, where the pose is represented by a center point and the offsets for each keypoint to the center point, and regard the regression results as the grouping cues to absorb the keypoints detected from the heatmaps, with the focus on improving the heatmap estimation and pixel-wise keypoint regression quality.

We combine the predicted keypoint heatmaps and the feature representation for pixel-wise keypoint regression. It differs from previous schemes that separate the heatmap estimation head and the pixel-wise keypoint regression head [45]. As a result, the heatmaps, whose quality is usually better than pixel-wise keypoint regression in terms of keypoint localization quality, provide strong guide to pixel-wise keypoint regression, leading higher keypoint regression quality.

We adopt a pixel-wise spatial transformer network, a simple extension of spatial transformer network [15], to adaptively learn the representation for handling the local transformation variance, such as human scale and orientation variance. This is motivated by that pixel-wise keypoint regression is an object-level (person) task and different persons in one image might have different scales and/or different orientations.

In addition, we present a joint shape and heatvalue scoring scheme to predict the degree that each pose estimation is a real pose. We use the scores to rank the final pose estimation results by demoting the mis-grouped poses (e.g., keypoints absorbed together but from different persons or the background). We also revisit the imbalance issue [32] between keypoint pixels and non-keypoint pixels, and simply reweigh the two kinds of pixels in the heatmap estimation loss, which improves the heatmap estimation quality significantly. We demonstrate the proposed approach with the state-of-the-art bottom-up human pose estimation performance on the COCO and CrowdPose benchmark. We obtain the AP score 70.2 for the single-scale testing on the COCO test-dev set and the AP score 66.2 on the CrowdPose test set.

2 RELATED WORK

The convolutional neural network solutions [1], [9], [11], [20], [26], [30], [35], [37] to human pose estimation have shown superior performance over the conventional methods, such as the probabilistic graphical model or the pictorial structure model [31],

• J. Wang is with Microsoft Research, Beijing, P.R. China.
E-mail: jingdw@microsoft.com



Fig. 1. Multi-person pose estimation. There are several key challenges for the bottom-up framework: unknown number of persons, diverse person scales and orientations, various poses, etc.

[44]. Recent advances show that the heatmap estimation based methods, estimating keypoint heatmaps [6], [7], [43] where the keypoints are localized, outperform the keypoint position prediction methods [3], [38].

Top-down methods. Representative works include: PoseNet [29], RMPE [10], convolutional pose machine [41], Hourglass [24], Mask R-CNN [12], and cascaded pose networks [4], simple baseline [42], and so on. The recently-developed HRNet [36], [40] achieves the significant gain, especially regarding keypoint localization accuracy. These methods exploit the advances in person detection as well as extra person bounding-box labeling information [17]. The keypoint heatmap estimation is eased as the background is largely removed and fewer confusing pixels are remained (in most cases there is only one instance for each keypoint) in the detection box. The top-down pipeline, however, takes extra cost in the person box detection.

Bottom-up methods. Most existing bottom-up methods mainly focus on how to associate the detected keypoints that belong to the same person together. The pioneering work, DeepCut [32] and DeeperCut [14], formulates the keypoint association problem as an integer linear program, which however takes longer processing time (e.g., the order of hours).

The OpenPose work [2], a real-time pose detector, developed the part-affinity field approach to link the keypoints that are likely to lie in the same person, which is extended in the PifPaf work [17]. The associative embedding approach [23] maps each keypoint to a scalar embedding so that the embeddings of the keypoints from the same person are close, and clusters the keypoints using the scalar embeddings. The PersonLab approach [28] introduces a greedy decoding scheme together with hough voting for grouping.

Several recent works [1], [27], [45] densely regress a set of pose candidates, where each candidate consists of the keypoint positions that might be from the same person, and then use the candidates as grouping cues to cluster the keypoints selected from the keypoint heatmaps into individuals. Our work belongs to this category and proposes to use heatmaps to guide pixel-wise keypoint regression. This guidance is in some sense related to some other methods, e.g., using part affinity fields to help predict heatmaps in OpenPose [2].

Additionally, we handle the scale and orientation diversity of different persons by a pixel-wise extension of spatial transformer network (STN) [15], pixel-wise STN. There are several related works, dense spatial transformer network [18], instance transformation network [39], and deformable GANs [34]. The first one, dense spatial transformer network [18], actually stills uses a global transformation (thin-plate spline). The second one is very close to ours, but applied to a different problem, text

detection. The third one is to conduct STN over different regions for alignment, which comes from the pose estimation results, while ours is for pixel-level representations and thus robust pose estimation. The feature pyramid network [21] and deformable convolutions [8], mainly developed for object detection, might have similar effect with pixel-wise STN. We choose pixel-wise STN because the implementation is easy without the necessity of distributing the objects of some scale into some pyramid level and it is more interpretable (explicitly model the scale and the orientation) compared to deformable convolutions.

3 APPROACH

Given an image I , multi-person pose estimation aims to predict a set of N human poses: $\{\mathcal{P}_1, \mathcal{P}_2, \dots, \mathcal{P}_N\}$, where the pose $\mathcal{P}_n = \{\mathbf{p}_{n1}, \mathbf{p}_{n2}, \dots, \mathbf{p}_{nK}\}$ consists of K keypoints belonging to the person n .

3.1 Formulation

The input image I is fed into a backbone network, outputting a representation F . The representation F goes through the heads, as depicted in Figure 2, with the outputs consisting of two parts: the keypoint heatmaps, and the pixel-wise keypoint regression results. The keypoint heatmaps H consist of K maps, $\mathbf{H}_1, \mathbf{H}_2, \dots, \mathbf{H}_K$. The heat value at each position for each keypoint heatmap indicates the degree that the keypoint lies in the position.

The pixel-wise keypoint regression results consist of two parts. One is the center heatmap C showing the degree that each position is the center of one pose. The offset maps, O , contain $2K$ maps and show the offsets of the keypoint to the center if the current position is a pose center.

Heatmap-guided pixel-wise keypoint regression. The keypoint heatmaps are estimated from the representation through a keypoint estimation head \mathcal{H} :

$$H = \mathcal{H}(F). \quad (1)$$

Unlike previous works [25], [27] that regress the center heatmap C and the pose coordinates O only from the representation F , we estimate them by exploring the estimated heatmaps through a pixel-wise keypoint regression head \mathcal{P} ,

$$(C, O) = \mathcal{P}(F, H). \quad (2)$$

There are two benefits. The keypoint positions by the pixel-wise keypoint regression are regressed more accurately as the estimated keypoint heatmaps, relatively more accurate than pixel-wise keypoint regression, provide strong guidance for regressing keypoint offsets. On the other hand, heatmap estimation, besides

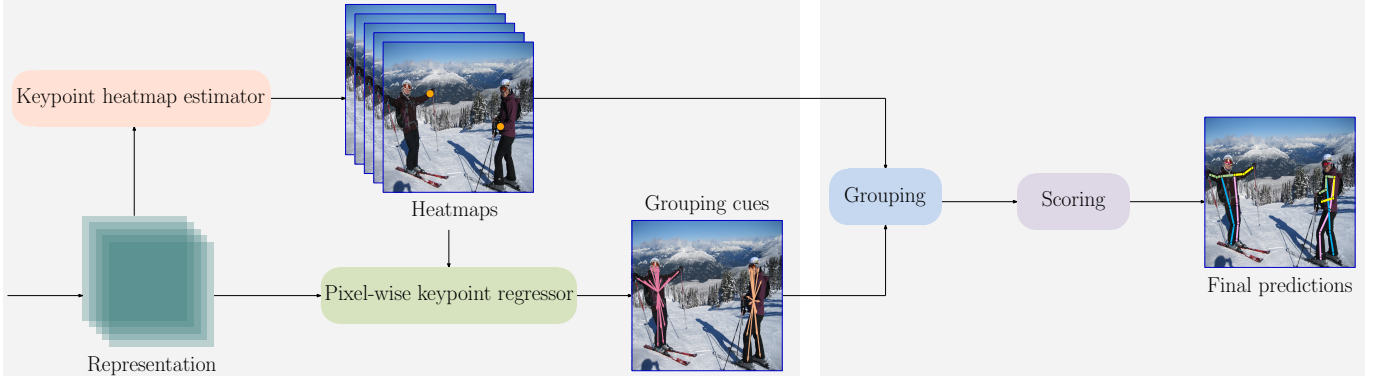


Fig. 2. Pipeline. The representation (F) output from a backbone goes into the keypoint heatmap estimator \mathcal{H} , outputting the keypoint heatmaps H. The representation, the concatenation of the heatmaps H and the input representation F, is fed into the pixel-wise keypoint regressor \mathcal{P} , outputting the offset maps O and the center heatmap C as the grouping cues. The keypoint candidates obtained from the keypoint heatmaps H are grouped with the help of the pixel-wise keypoint regression results O and C, followed by a scoring stage generating the final pose predictions.

the heatmap supervision, gets additional supervision from the pixel-wise keypoint regression target.

Adaptive representation transformation. To address the scale and orientation variance, i.e., different persons in an image might have different sizes and different orientations, we propose an adaptive representation transformation (ART) unit that consists of an adaptive convolution followed by BN and ReLU. The adaptive convolution is a modification of a normal convolution: $\mathbf{y}(\mathbf{q}) = \sum_{i=1}^9 \mathbf{W}_i \mathbf{x}(\mathbf{g}_{si} + \mathbf{q})$. Here, \mathbf{q} is a 2D position, $\{\mathbf{g}_{s1}, \mathbf{g}_{s2}, \dots, \mathbf{g}_{s9}\}$ (denoted by a 2×9 matrix \mathbf{G}_s) are 2D offsets, and $\{\mathbf{W}_1, \mathbf{W}_2, \dots, \mathbf{W}_9\}$ are the kernel weights. This modification is similar to deformable convolutions [8], but we compute the offsets by explicitly modeling local scale and orientation.

We compute the offsets \mathbf{G}_s : $\mathbf{G}_s = \mathbf{T}\mathbf{G}_t$, by estimating a local inverse affine transformation $\mathbf{T} \in \mathbb{R}^{2 \times 2}$ that characterizes local scaling and rotation for each position \mathbf{q} so that in the transformed space a convolution is conducted with the regular 3×3 positions, i.e., the offsets in a matrix form are:

$$\mathbf{G}_t = \begin{bmatrix} -1 & 0 & 1 & -1 & 0 & 1 & -1 & 0 & 1 \\ -1 & -1 & -1 & 0 & 0 & 0 & 1 & 1 & 1 \end{bmatrix}. \quad (3)$$

We estimate the local transformation \mathbf{T} by extending spatial transformer network [15] from a global manner to a pixel-wise manner, for each position through a 3×3 convolution with the weights shared by all the positions.

In our implementation, the keypoint heatmap estimation head \mathcal{H} consists of two adaptive representation transformation units and a subsequent linear transformation outputting the keypoint heatmaps H. The pixel-wise keypoint regression head feeds the concatenation of F and H into two adaptive representation transformation units and a subsequent linear transformation outputting the center heatmap C and the offset maps O.

Loss function. The loss contains two parts: keypoint heatmap estimation loss and pixel-wise keypoint regression loss. We use a tradeoff heatmap estimation loss to balance the keypoint region and the non-keypoint region. The loss function is formulated as the weighted distances between the predicted heat values and the groundtruth heat values:

$$\ell_h = \|\mathbf{M} \odot (\mathbf{H} - \mathbf{H}^*)\|_2^2. \quad (4)$$

Here, $\|\cdot\|_2$ is the entry-wise 2-norm. \odot is the element-wise product operation. \mathbf{M} corresponds K masks, and the size is $H \times W \times K$.

The k th mask, \mathbf{M}_k , is formed so that the mask weight of the positions not lying in the k th keypoint region is 0.1, and others are 1.

We use the normalized smooth loss to form the pixel-wise keypoint regression loss:

$$\ell_p = \sum_{i \in \mathcal{C}} \frac{1}{Z_i} \text{smooth}_{L_1}(\mathbf{o}_i - \mathbf{o}_i^*) + \|\mathbf{C} - \mathbf{C}^*\|_2^2. \quad (5)$$

Here, $Z_i = \sqrt{H_i^2 + W_i^2}$ is the size of the corresponding person instance and H_i and W_i are the height and the width of the instance box. i is a position lying in a center region, and \mathcal{C} is the set of the positions lying in some center region. \mathbf{o}_i (\mathbf{o}_i^*), a column of the offset maps O (\mathbf{O}^*) is the $2K$ -dimensional (groundtruth) offset vector for the position i . \mathbf{C}^* is the groundtruth center heatmap.

The whole loss function is the sum of the losses:

$$\ell = \ell_h + \lambda \ell_p, \quad (6)$$

where λ is a weight. In our implementation, we consider that the pixel-wise keypoint regression only provides a grouping cue, and set $\lambda = 0.01$, a smaller weight for the pixel-wise keypoint regression loss.

Training data construction. We need to construct the training data for two parts: the keypoint heatmaps, as well as the offset maps and the center heatmap. We generate the groundtruth keypoint heatmaps \mathbf{H}^* for each training image. The groundtruth keypoint heatmaps \mathbf{H}^* contains K maps, and each map corresponds to one keypoint type. We build them as done in [23]: assigning a heat value using the Gaussian function centered at a point around each groundtruth keypoint.

The groundtruth offset maps and the groundtruth center heatmap are constructed from $\{\mathcal{P}_1, \mathcal{P}_2, \dots, \mathcal{P}_N\}$. We use the n th pose \mathcal{P}_n as an example and others are the same. We compute the center position $\bar{\mathbf{p}}_n = \frac{1}{K} \sum_{k=1}^K \mathbf{p}_{nk}$ and the offsets $\mathcal{T}_n = \{\mathbf{p}_{n1} - \bar{\mathbf{p}}_n, \mathbf{p}_{n2} - \bar{\mathbf{p}}_n, \dots, \mathbf{p}_{nK} - \bar{\mathbf{p}}_n\}$ as the target. We use an expansion scheme to augment the center point to the center region: $\{\mathbf{m}_n^1, \mathbf{m}_n^2, \dots, \mathbf{m}_n^M\}$, which are central positions around the pose center $\bar{\mathbf{p}}_n$ with the radius 4, and accordingly update the offsets. Each central position \mathbf{m}_n^m has a confidence value c_n^m indicating how confident it is the center and computed using the way forming the heatmap, which results in a so-called

center heatmap \mathbf{C}^* ¹. The positions not lying in the region have zero heat value, and accordingly it have no offset values. The offset maps are denoted by \mathbf{O}^* .

3.2 Inference

Grouping. Given an image from which we want to predict the human poses, we compute the keypoint heatmaps \mathbf{H} and the pixel-wise keypoint regression results (\mathbf{C}, \mathbf{O}) . We use non-maximum suppression to find several (30 in our implementation) keypoint candidates, $\mathcal{S} = \{\mathcal{S}_1, \mathcal{S}_2, \dots, \mathcal{S}_K\}$, with each set \mathcal{S}_k consisting of the k th keypoint candidates from the keypoint heatmaps \mathbf{H} , and remove the keypoint candidates whose heatvalues are too small (smaller than 0.01). We also use non-maximum suppression to filter out pixel-wise keypoint regression results using the center heatmap, leading to a set of M ($M = 30$, in our implementation) regression results, $\mathcal{G}_1, \dots, \mathcal{G}_M$, where each result \mathcal{G}_m contains K keypoints.

We group the keypoint candidates \mathcal{S} by regarding each pixel-wise keypoint regression result \mathcal{G}_m as a grouping cue. For each keypoint, e.g., \mathbf{p}_k , in each group cue \mathcal{G}_m , we absorb the closest keypoint candidate among the candidates \mathcal{S}_k with the same keypoint type if their distance is within 75 pixels, and otherwise use \mathbf{p}_k as the k th keypoint to form the m th pose candidate $\bar{\mathcal{G}}_m$. The K keypoint candidates absorbed to \mathcal{G}_m form a final pose candidate $\bar{\mathcal{G}}_m$.

Scoring. Given a candidate pose $\bar{\mathcal{G}} = \{\mathbf{p}_1, \mathbf{p}_2, \dots, \mathbf{p}_K\}$ and the center point \mathbf{p} predicting its grouping cue \mathcal{G} , the naive scoring scheme is $\frac{1}{K} \sum_k h_k(\mathbf{p}_k) o(\mathbf{p})$, where $o(\mathbf{p})$ is the heatvalue of \mathbf{p} from the center heatmap \mathbf{O} , and $h_k(\mathbf{p}_k)$ is the keypoint heatvalue from the k th keypoint heatmap \mathbf{H}_k .

This naive scoring scheme does not consider the spatial information, and the space remains for improvement. Partially inspired by [33], which suggests using a graphical model to capture the spatial relation or using a validation set to learn to combine different scores, we instead learn a small network to predict the OKS score for each candidate pose $\bar{\mathcal{G}}$ according to the keypoint heatvalues, $h_1(\mathbf{p}_1), h_2(\mathbf{p}_2), \dots, h_K(\mathbf{p}_K)$, helpful for indicating the visibility, as well as the shape feature. The shape feature includes the distance and the relative offset between a pair of neighboring keypoints. A neighboring pair (i, j) corresponds to a stick in the COCO dataset, and there are 19 sticks (denoted by \mathcal{E}) in the COCO dataset. The shape feature is denoted as: $\{d_{ij} | (i, j) \in \mathcal{E}\}$ and $\{\mathbf{p}_i - \mathbf{p}_j | (i, j) \in \mathcal{E}\}$. The resulting whole feature consists 74 dimension for the COCO dataset.

We use a small network, consisting two fully-connected layers (each followed by a ReLU layer), and a linear prediction layer, for learning the OKS score for a candidate $\bar{\mathcal{G}}$, with the real OKS as the target. We use the pose candidates obtained after grouping over the COCO train2017 dataset to form the training examples. During inference, we feed the shape and heatvalue feature into the small network getting the score for each pose candidate. This scoring scheme is helpful to promote the pose candidates that are more likely to be true pose.

4 EXPERIMENTS

4.1 Setting

Dataset. We evaluate our approach on the COCO keypoint detection task [22]. The train2017 set includes 57K images and

1. In case that one position belongs to two or more central regions, we choose only one central region whose center is the closest to that position.

TABLE 1
GFLOPs and #parameters of the representative top competitors and our approaches with the backbones: HRNet-W32 (H-W32), HRNet-W48 (H-W48) and HrHRNet-W48 (Hr-W48). AE-HG = associative embedding-Hourglass.

	AE-HG	PersonLab	HrHRNet	H-W32	H-W48	Hr-W48
Input size	512	1401	640	512	640	640
#param. (M)	227.8	68.7	63.8	30.7	66.8	66.9
GFLOPs	206.9	405.5	154.3	63.7	170.1	179.5

150K person instances annotated with 17 keypoints, the val2017 set contains 5K images, and the test-dev2017 set consists of 20K images. We train the models on the train2017 set and report the results on the val2017 and test-dev2017 sets.

Evaluation metric. The standard average precision and recall based on Object Keypoint Similarity (OKS) are adopted as the evaluation metrics. Object Keypoint Similarity (OKS): $OKS = \frac{\sum_i \exp(-d_i^2/2s^2k_i^2)\delta(v_i>0)}{\sum_i \delta(v_i>0)}$, where d_i is the Euclidean distance between each corresponding ground truth and the detected keypoint, v_i is the visibility flag of the ground truth, s is the object scale, and k_i is a per-keypoint constant that controls falloff. We report the following metrics²: AP (the mean of AP scores at OKS = 0.50, 0.55, ..., 0.90, 0.95), AP⁵⁰ (AP at OKS = 0.50), AP⁷⁵ (AP at OKS = 0.75), AP^M for medium objects, AP^L for large objects, and AR (the mean of AR scores at OKS = 0.50, 0.55, ..., 0.90, 0.95), AR⁵⁰ (AR at OKS = 0.50), AR⁷⁵ (AR at OKS = 0.75), AR^M for medium objects, AR^L for large objects.

Training. The data augmentation follows [23] and includes random rotation ($[-30^\circ, 30^\circ]$), random scale ($[0.75, 1.5]$) and random translation ($[-40, 40]$). We conduct the image cropping to 512×512 (for HRNet-W32) or 640×640 (for HRNet-W48 and HrHRNet-W48) with random flipping as training samples.

We use the Adam optimizer [16]. The base learning rate is set as $1e-3$, and is dropped to $1e-4$ and $1e-5$ at the 90th and 120th epochs, respectively. The training process is terminated within 140 epochs.

Testing. We resize the short side of the images to 512/640 and keep the aspect ratio between height and width. Following [23], we adopt three scales 0.5, 1 and 2 in multi-scale testing and compute the heatmap and pose positions by averaging the heatmaps and pixel-wise keypoint regressions of the original and flipped images.

4.2 Results

Validation results. Table 2 shows the comparisons of our method and other state-of-the-art methods. We use HRNet-W32 and HRNet-W48 as the backbones and adopt three parallel branches each estimating the keypoint heatmap. We average the three output heatmaps as the final heatmap prediction that, as a part of input, is fed into the pixel-wise keypoint regressor. We also test the performance using HrHRNet-W48 as the backbone³ Table 1 presents the parameter and computation complexities for our approach and the representative top competitors, AE-Hourglass [23], PersonLab [28] and HrHRNet [5].

2. <http://cocodataset.org/#keypoints-eval>

3. We perform keypoint heatmap estimation and pixel-wise keypoint regression over the $4\times$ representation for generating the grouping cues. We use the $2\times$ resolution representation in HrHRNet-W48 to estimate $2\times$ resolution heatmaps, and find the keypoint candidates from the $2\times$ resolution heatmaps for the further grouping.

TABLE 2
Comparisons on the COCO validation set. * means using refinement. AE: Associative Embedding [23].

Method	Input size	AP	AP ⁵⁰	AP ⁷⁵	AP ^M	AP ^L	AR	AR ^M	AR ^L
single-scale testing									
CenterNet-DLA [45]	512	58.9	—	—	—	—	—	—	—
CenterNet-HG [45]	512	64.0	—	—	—	—	—	—	—
PifPaf [17]	—	67.4	—	—	—	—	—	—	—
PersonLab [28]	601	54.1	76.4	57.7	40.6	73.3	57.7	43.5	77.4
PersonLab [28]	1401	66.5	86.2	71.9	62.3	73.2	70.7	65.6	77.9
HrHRNet-W32 + AE [5]	512	67.1	86.2	73.0	—	—	—	61.5	76.1
HrHRNet-W48 + AE [5]	640	69.9	87.2	76.1	—	—	—	65.4	76.4
Ours (HRNet-W32)	512	67.8	86.8	74.0	62.0	76.4	72.3	65.6	82.0
Ours (HRNet-W48)	640	70.1	88.1	76.0	65.6	77.2	74.8	69.2	82.9
Ours (HrHRNet-W48)	640	71.3	88.4	77.0	67.5	77.3	75.8	70.9	83.1
multi-scale testing									
Deep body-foot [13]	480	66.4	—	—	—	—	—	—	—
HrHRNet-W32 + AE [5]	512	69.9	87.1	76.0	—	—	—	65.3	77.0
HrHRNet-W48 + AE [5]	640	72.1	88.4	78.2	—	—	—	67.8	78.3
Ours (HRNet-W32)	512	70.7	88.0	76.9	66.1	77.7	75.8	70.2	83.8
Ours (HRNet-W48)	640	72.5	88.9	78.7	68.9	78.2	77.7	72.8	84.7
Ours (HrHRNet-W48)	640	72.9	89.2	78.8	69.3	78.5	78.2	73.2	85.4

TABLE 3
Comparisons on the COCO test-dev set. * means using refinement. AE: Associative Embedding.

Method	Input size	AP	AP ⁵⁰	AP ⁷⁵	AP ^M	AP ^L	AR	AR ^M	AR ^L
single-scale testing									
OpenPose* [2]	—	61.8	84.9	67.5	57.1	68.2	66.5	—	—
AE [23]	512	56.6	81.8	61.8	49.8	67.0	—	—	—
CenterNet-DLA [45]	512	57.9	84.7	63.1	52.5	67.4	—	—	—
CenterNet-HG [45]	512	63.0	86.8	69.6	58.9	70.4	—	—	—
PifPaf [17]	—	66.7	—	—	62.4	72.9	—	—	—
SPM* [27]	-	66.9	88.5	72.9	62.6	73.1	—	—	—
PersonLab [28]	1401	66.5	88.0	72.6	62.4	72.3	71.0	66.1	77.7
HrHRNet-W48 + AE [5]	640	68.4	88.2	75.1	64.4	74.2	—	—	—
Ours (HRNet-W32)	512	66.6	87.8	72.8	61.1	74.5	71.4	64.6	80.8
Ours (HRNet-W48)	640	69.4	88.9	76.2	64.9	75.7	74.3	68.5	82.2
Ours (HrHRNet-W48)	640	70.2	89.5	77.3	66.5	75.6	75.1	70.1	82.1
multi-scale testing									
AE [23]	512	63.0	85.7	68.9	58.0	70.4	—	—	—
AE* [23]	512	65.5	86.8	72.3	60.6	72.6	70.2	64.6	78.1
PersonLab [28]	1401	68.7	89.0	75.4	64.1	75.5	75.4	69.7	83.0
HrHRNet-W48 + AE [5]	640	70.5	89.3	77.2	66.6	75.8	—	—	—
Ours (HRNet-W32)	512	69.4	88.9	76.2	64.9	75.8	74.9	69.1	82.9
Ours (HRNet-W48)	640	71.4	89.8	78.3	67.8	76.8	76.9	71.7	84.1
Ours (HrHRNet-W48)	640	71.8	90.2	78.7	68.3	76.8	77.4	72.4	84.3

TABLE 4
Ablation study: heatmap-guided pixel-wise keypoint regression, heatmap tradeoff loss, adaptive representation transformation (ART) and scoring. Scoring only affects the overall quality.

Heatmap guidance	Tradeoff loss	Adaptive representation	Scoring	Regression quality	Heatmap quality	Final quality
				59.6	71.3	64.5
✓				60.5	71.8	64.9
✓	✓			61.5	73.2	66.2
✓	✓	✓		65.1	73.3	67.2
✓	✓	✓	✓	65.1	73.3	67.8

Our approach, using HRNet-W32 as the backbone, achieves 67.8 AP score. Compared to the methods with similar GFLOPs,

CenterNet-DLA [45] and PersonLab [28] (with the input size 601), our approach achieves over 8.9 improvement. In comparison to CenterNet-HG [45] whose model size is far larger than HRNet-W32, our gain is 3.8, consisting of two aspects: (1) 0.6⁴ from our baseline (our baseline using HRNet-W32 as the backbone achieves 64.6 (Table 4) (2) the remaining gain 3.2 from our methodology (Table 4).

Our approach benefits from large input size, large model size and higher resolution representations. Our approach, with HRNet-W48 as the backbone, the input size 640, obtains the best performance 70.1 and 2.3 gain over HRNet-W32. Compared

4. In the gain 0.6, 0.3 comes from using the average of keypoint positions as the center position compared to using the human box center [45].

with state-of-the-art methods, our approach gets 6.1 gain over CenterNet-HG, 3.6 gain over PersonLab (the input size 1401), and 2.7 gain over PifPaf [17] whose GFLOPs are more than twice as many as ours. Besides, we use the higher resolution representation (HrHRNet-W48 [5]), leading to 1.2 gain over HRNet-W48.

Following [23], [28], we report the results with multi-scale testing. This brings about 2.9 gain for HRNet-W32, 2.4 gain for HRNet-W48 and 1.6 points for HrHRNet-W48.

Test-dev results. The results of our approach and other state-of-the-art methods on the test-dev dataset are presented in Table 3.

Our approach with HRNet-W32 as the backbone achieves 66.6 AP scores, and significantly outperforms the methods with the similar model size. Our approach with HrHRNet-W48 as the backbone gets the best performance 70.2, leading to 3.7 gain over PersonLab, 3.5 gain over PifPaf [17], and 1.8 gain over HrHRNet [5]. With multi-scale testing, our approach with HRNet-W32 as the backbone achieves 69.4, even better than PersonLab with a much larger model size. Our approach with HrHRNet-W48 achieves 71.8 AP score, much better than associative embedding [23], 3.1 gain over PersonLab, and 1.3 gain over HrHRNet [5].

4.3 Ablation Study

We study the effects of the components in our approach: heatmap-guided pixel-wise keypoint regression, heatmap tradeoff loss, adaptive representation transformation, and pose scoring. We check three qualities: pixel-wise keypoint regression quality, heatmap estimation quality, and final quality. The first one is obtained by directly using the regression results and evaluating it using the AP scores. The second one is done by grouping keypoints identified from heatmaps using the groundtruth poses as the grouping cue (i.e., replacing the regressed poses). The final quality is the quality of the whole scheme of our approach.

The ablation study result is presented in Table 4. The heatmap guidance scheme indeed boosts pixel-wise keypoint regression: the improvements is 0.9. The final quality is improved by 0.4. The heatmap tradeoff loss improves the heatmap quality greatly (by 1.4). The adaptive representation transformation improves the pixel-wise keypoint regression quality (by 3.6), and the final results (by 1.0). The scoring scheme ranks the final estimations and achieves a gain 0.6.

Figure 4 illustrates the error analysis results for pixel-wise keypoint regression (a - d), keypoint heatmap estimation (e - h) and final predictions (i - l). The detailed analysis is given in the following.

Error analysis. We analyze how each component contributes to the performance improvement by using the coco analysis tool [33]. Four error types are studied: (i) *Jitter* error: small localization error around the correct keypoint location; (ii) *Miss* error: large localization error, the detected keypoint is not within the proximity of any ground truth keypoint of any instance; (iii) *Inversion* error: confusion between keypoints within a instance. The detected keypoint is in the proximity of a wrong ground truth keypoint belonging to the same instance. (iv) *Swap* error: confusion between keypoints of different instances. The detected keypoint is in the proximity of a ground truth keypoint belonging to a different instance. The detailed definitions are in [33].

Heatmap guidance: The comparison between Figure 4 (a) and Figure 4 (b) shows that exploiting the heatmap for pixel-wise keypoint regression brings about improvement for all the errors.

TABLE 5
Comparisons on the CrowdPose test set. * means using refinement. AE: Associative Embedding.

Method	Input size	AP	AP ⁵⁰	AP ⁷⁵	AP ^E	AP ^M	AP ^H
top-down methods							
Mask R-CNN [12]	—	57.2	83.5	60.3	69.4	57.9	45.8
AlphaPose [10]	—	61.0	81.3	66.0	71.2	61.4	51.1
SPPE* [19]	—	66.0	84.2	71.5	75.5	66.3	57.4
bottom-up methods: single-scale testing							
OpenPose [2]	—	—	—	—	62.7	48.7	32.3
HrHRNet-W48 + AE [5]	640	65.9	86.4	70.6	73.3	66.5	57.9
Ours (HRNet-W32)	512	64.9	84.5	69.6	72.7	65.5	56.1
Ours (HRNet-W48)	640	66.1	84.6	71.2	73.4	66.9	57.1
Ours (HrHRNet-W48)	640	66.2	84.9	71.4	73.6	67.0	57.6
bottom-up methods: multi-scale testing							
HrHRNet-W48 + AE [5]	640	67.6	87.4	72.6	75.8	68.1	58.9
Ours (HRNet-W32)	512	67.5	86.1	72.6	75.5	68.2	58.2
Ours (HRNet-W48)	640	68.2	85.7	73.4	75.9	69.0	58.9
Ours (HrHRNet-W48)	640	68.2	86.2	73.6	75.8	69.1	59.1

The comparison between Figure 4 (e) and Figure 4 (f), shows the heatmap estimation quality improvement, indicating that exploiting the heatmap for improving pixel-wise keypoint regression in turns benefits the heatmap estimation, though the improvement is not as great as pixel-wise keypoint regression.

Heatmap tradeoff loss: The tradeoff aims to balance the numbers of the keypoint pixels and the non-keypoint pixels, mainly for keypoint heatmap estimation. This is able to strengthen the keypoint classification capability. By comparing Figure 4 (g) and Figure 4 (f), we can see that the missing error is reduced the greatest (by 0.5). This is as expected, and the error reduction mainly comes from the classification capability. Because of the assistance from the high-quality heatmaps, the pixel-wise keypoint regression quality is also improved as seen in Figure 4 (c).

Adaptive representation transformation: The comparison between Figure 4 (d) and Figure 4 (c) shows that the pixel-wise keypoint regression quality is largely improved, mainly on the jitter error and the missing error. Figure 3 illustrates the sampled 9 positions at the pose center computed by the pixel-wise STN for the pixel-wise keypoint regression head, which shows that the human scale and the human rotation are captured by the adaption scheme. The adaption scheme helps improve the pixel-wise representation by seeing the global context instead of the local context in a regular convolution.

4.4 CrowdPose

Dataset. We evaluate our approach on the CrowdPose [19] dataset that is more challenging and includes many crowded scenes. The train set contains 10K images, the val set includes 2K images and the test set consists of 20K images. We train our models on the CrowdPose train and val sets and report the results on the test set as done in [5].

Evaluation metric. The standard average precision based on Object Keypoint Similarity (OKS) which is the same as COCO are adopted as the evaluation metrics. The CrowdPose dataset is split into three crowding levels: easy, medium, hard. We report the following metrics: AP, AP⁵⁰, AP⁷⁵, AP^E for easy images, AP^M for medium images, AP^H for hard images.

Training and Testing. The train and test methods follow COCO except the training epochs. We use the Adam optimizer [16]. The base learning rate is set as 1e−3, and is dropped to 1e−4 and



Fig. 3. Illustrating the pixel-wise STN contained in the pixel-wise keypoint regression head. We show the 9 positions learned from pixel-wise STN at the pose center.

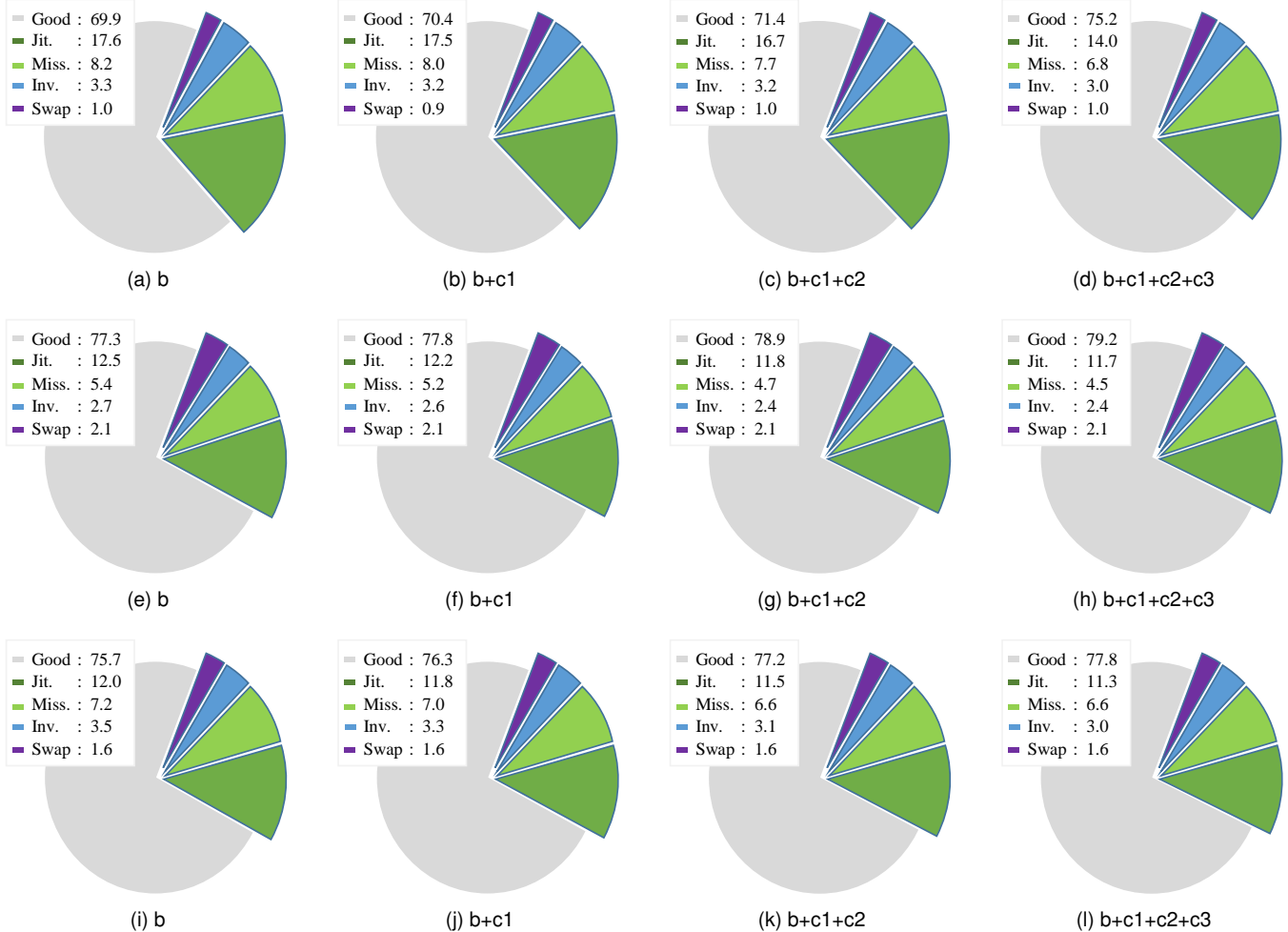


Fig. 4. Component analysis in terms of four errors for three qualities: (a) - (d): pixel-wise keypoint regression; (e) - (h): keypoint heatmap estimation; (i) - (l): final poses. b: the baseline corresponding to the 64.6 AP score in Table 4; c1: heatmap guided pixel-wise keypoint estimation; c2: heatmap tradeoff loss; c3: adaptive representation transformation.

1e-5 at the 200th and 260th epochs, respectively. The training process is terminated within 300 epochs.

Test set results. The results of our approach and other state-of-the-art methods on the test set are showed in Table 5. Our approach with HRNet-W48 as the backbone achieves 66.1 AP, and outperforms the top-down methods, leading to 8.9 gain over Mask R-CNN [12], 5.1 gain over AlphaPose [10]. With multi-scale testing, our approach with HRNet-W48 as the backbone gets the best performance 68.2 AP score, much better than OpenPose [2], 2.2 gain over SPPE, and 0.6 gain over HrHRNet [5].

5 CONCLUSIONS

We present a baseline approach for improving bottom-up human pose estimation quality. The success comes from: exploiting the

heatmaps for guiding pixel-wise keypoint regression, adaptive representation transformation (ART) for handling the diversity of human scales and rotations and better pixel-wise keypoint regression, heatmap tradeoff loss for improving heatmap estimation quality, learning to scoring for promoting the pose candidates that are more likely to be true poses.

REFERENCES

- [1] 1, 2
- [2] Z. Cao, T. Simon, S. Wei, and Y. Sheikh. Realtime multi-person 2d pose estimation using part affinity fields. In *CVPR*, pages 1302–1310, 2017. 1, 2, 5, 6, 7
- [3] J. Carreira, P. Agrawal, K. Fragkiadaki, and J. Malik. Human pose estimation with iterative error feedback. In *CVPR*, pages 4733–4742, 2016. 2



Fig. 5. Qualitative results of some example images on COCO.

- [4] Y. Chen, Z. Wang, Y. Peng, Z. Zhang, G. Yu, and J. Sun. Cascaded pyramid network for multi-person pose estimation. In *CVPR*, pages 7103–7112, 2018. 2
- [5] B. Cheng, B. Xiao, J. Wang, H. Shi, T. S. Huang, and L. Zhang. Higherhmet: Scale-aware representation learning for bottom-up human pose estimation. In *The IEEE/CVF Conference on Computer Vision and Pattern Recognition (CVPR)*, June 2020. 4, 5, 6, 7
- [6] X. Chu, W. Ouyang, H. Li, and X. Wang. Structured feature learning for pose estimation. In *CVPR*, pages 4715–4723, 2016. 2
- [7] X. Chu, W. Yang, W. Ouyang, C. Ma, A. L. Yuille, and X. Wang. Multi-context attention for human pose estimation. In *CVPR*, pages 5669–5678, 2017. 2
- [8] J. Dai, H. Qi, Y. Xiong, Y. Li, G. Zhang, H. Hu, and Y. Wei. Deformable convolutional networks. In *ICCV*, pages 764–773, 2017. 2, 3
- [9] X. Fan, K. Zheng, Y. Lin, and S. Wang. Combining local appearance and holistic view: Dual-source deep neural networks for human pose estimation. In *CVPR*, pages 1347–1355, 2015. 1
- [10] H. Fang, S. Xie, Y. Tai, and C. Lu. RMPE: regional multi-person pose estimation. In *ICCV*, pages 2353–2362, 2017. 2, 6, 7
- [11] G. Gkioxari, A. Toshev, and N. Jaitly. Chained predictions using convolutional neural networks. In *ECCV*, pages 728–743, 2016. 1
- [12] K. He, G. Gkioxari, P. Dollár, and R. B. Girshick. Mask R-CNN. In *ICCV*, pages 2980–2988, 2017. 2, 6, 7
- [13] G. Hidalgo, Y. Raaj, H. Idrees, D. Xiang, H. Joo, T. Simon, and Y. Sheikh. Single-network whole-body pose estimation. In *ICCV*, 2019. 1, 5
- [14] E. Insafutdinov, L. Pishchulin, B. Andres, M. Andriluka, and B. Schiele. Deeppcut: A deeper, stronger, and faster multi-person pose estimation model. In *ECCV*, pages 34–50, 2016. 2
- [15] M. Jaderberg, K. Simonyan, A. Zisserman, and K. Kavukcuoglu. Spatial transformer networks. In *NIPS*, pages 2017–2025, 2015. 1, 2, 3
- [16] D. P. Kingma and J. Ba. Adam: A method for stochastic optimization. *CoRR*, abs/1412.6980, 2014. 4, 6
- [17] S. Kreiss, L. Bertoni, and A. Alahi. Pifpaf: Composite fields for human pose estimation. In *CVPR*, pages 11977–11986, 2019. 2, 5, 6
- [18] J. Li, Y. Chen, L. Cai, I. Davidson, and S. Ji. Dense transformer networks for brain electron microscopy image segmentation. In *IJCAI, 2019*, pages 2894–2900, 2019. 2
- [19] J. Li, C. Wang, H. Zhu, Y. Mao, H.-S. Fang, and C. Lu. Crowdpose: Efficient crowded scenes pose estimation and a new benchmark. *arXiv preprint arXiv:1812.00324*, 2018. 6
- [20] I. Lifshitz, E. Fetaya, and S. Ullman. Human pose estimation using deep consensus voting. In *ECCV*, pages 246–260, 2016. 1
- [21] T. Lin, P. Dollár, R. B. Girshick, K. He, B. Hariharan, and S. J. Belongie. Feature pyramid networks for object detection. In *CVPR*, pages 936–944, 2017. 2
- [22] T. Lin, M. Maire, S. J. Belongie, J. Hays, P. Perona, D. Ramanan, P. Dollár, and C. L. Zitnick. Microsoft COCO: common objects in context. In *ECCV*, pages 740–755, 2014. 4
- [23] A. Newell, Z. Huang, and J. Deng. Associative embedding: End-to-end learning for joint detection and grouping. In *NIPS*, pages 2274–2284, 2017. 1, 2, 3, 4, 5, 6
- [24] A. Newell, K. Yang, and J. Deng. Stacked hourglass networks for human pose estimation. In *ECCV*, pages 483–499, 2016. 2
- [25] X. Nie, J. Feng, J. Xing, and S. Yan. Pose partition networks for multi-person pose estimation. In *ECCV*, September 2018. 2
- [26] X. Nie, J. Feng, Y. Zuo, and S. Yan. Human pose estimation with parsing induced learner. In *CVPR*, June 2018. 1
- [27] X. Nie, J. Zhang, S. Yan, and J. Feng. Single-stage multi-person pose machines. *CoRR*, abs/1908.09220, 2019. 2, 5
- [28] G. Papandreou, T. Zhu, L. Chen, S. Gidaris, J. Tompson, and K. Murphy. Personlab: Person pose estimation and instance segmentation with a bottom-up, part-based, geometric embedding model. In *ECCV*, pages 282–299, 2018. 2, 4, 5, 6
- [29] G. Papandreou, T. Zhu, N. Kanazawa, A. Toshev, J. Tompson, C. Bregler, and K. Murphy. Towards accurate multi-person pose estimation in the wild. In *CVPR*, pages 3711–3719, 2017. 2
- [30] X. Peng, Z. Tang, F. Yang, R. S. Feris, and D. Metaxas. Jointly optimize data augmentation and network training: Adversarial data augmentation in human pose estimation. In *CVPR*, June 2018. 1
- [31] L. Pishchulin, M. Andriluka, P. V. Gehler, and B. Schiele. Poselet conditioned pictorial structures. In *CVPR*, pages 588–595, 2013. 1
- [32] L. Pishchulin, E. Insafutdinov, S. Tang, B. Andres, M. Andriluka, P. V. Gehler, and B. Schiele. Deeppcut: Joint subset partition and labeling for multi-person pose estimation. In *CVPR*, pages 4929–4937, 2016. 1, 2
- [33] M. R. Ronchi and P. Perona. Benchmarking and error diagnosis in multi-instance pose estimation. In *ICCV*, pages 369–378, 2017. 4, 6
- [34] A. Siarohin, E. Sangineto, S. Lathuilière, and N. Sebe. Deformable gans for pose-based human image generation. In *CVPR*, pages 3408–3416, 2018. 2
- [35] K. Sun, C. Lan, J. Xing, W. Zeng, D. Liu, and J. Wang. Human pose estimation using global and local normalization. In *ICCV*, pages 5600–5608, 2017. 1
- [36] K. Sun, B. Xiao, D. Liu, and J. Wang. Deep high-resolution representation learning for human pose estimation. In *CVPR*, pages 5693–5703, 2019. 2
- [37] W. Tang, P. Yu, and Y. Wu. Deeply learned compositional models for human pose estimation. In *ECCV*, September 2018. 1
- [38] A. Toshev and C. Szegedy. Deeppose: Human pose estimation via deep neural networks. In *CVPR*, pages 1653–1660, 2014. 2
- [39] F. Wang, L. Zhao, X. Li, X. Wang, and D. Tao. Geometry-aware scene text detection with instance transformation network. In *CVPR*, pages 1381–1389, 2018. 2
- [40] J. Wang, K. Sun, T. Cheng, B. Jiang, C. Deng, Y. Zhao, D. Liu, Y. Mu, M. Tan, X. Wang, W. Liu, and B. Xiao. Deep high-resolution representation learning for visual recognition. *IEEE Transactions on Pattern Analysis and Machine Intelligence*, pages 1–1, 2020. 2
- [41] S. Wei, V. Ramakrishna, T. Kanade, and Y. Sheikh. Convolutional pose machines. In *CVPR*, pages 4724–4732, 2016. 2
- [42] B. Xiao, H. Wu, and Y. Wei. Simple baselines for human pose estimation and tracking. In *ECCV*, pages 472–487, 2018. 2
- [43] W. Yang, W. Ouyang, H. Li, and X. Wang. End-to-end learning of deformable mixture of parts and deep convolutional neural networks for human pose estimation. In *CVPR*, pages 3073–3082, 2016. 2
- [44] Y. Yang and D. Ramanan. Articulated pose estimation with flexible mixtures-of-parts. In *CVPR*, pages 1385–1392, 2011. 1
- [45] X. Zhou, D. Wang, and P. Krähenbühl. Objects as points. *CoRR*, abs/1904.07850, 2019. 1, 2, 5